

Metrology of Individual Small Viruses

Kun Li, Arjav Shah, Rajesh Kumar Sharma, Raymond Adkins, Tihomir Marjanovic, Patrick S. Doyle,* and Slaven Garaj*

Viruses come in various shapes and sizes, and understanding their morphology is central to understanding their activity and function. The need for fast recognition and real-time fingerprinting methods for pathogenic viruses is a critical bottleneck in implementing many diagnostic and therapeutic techniques. In this work, nanopore tomography (NT) is implemented for fast measurements of the characteristic dimensions of viruses and the optimal operating conditions are explored. Using a small filamentous bacteriophage as a model, it is demonstrated that NT can detect geometrical features in a few-nanometer regime, with high throughput and accuracy, in aqueous conditions. The instrumental parameters are optimized to obtain virus diameter measurements that are robust to the uncertainties of the external parameters. Furthermore, NT is critically compared to various single-particle imaging techniques, with a particular emphasis on emerging helium ion microscopy (HIM). It is shown that, with proper operating procedures, HIM can reach a nanometer-scale resolution in viral metrology, while retaining a high throughput second only to NT. The high throughput of both techniques can foster sufficient statistics for a precise exploration of viral heterogeneity.

and eukaryotic cells – are important to understanding their activity, function, and heterogeneity.^[1] Viruses come in variable sizes and shapes, varying widely in the number and nature of their constituent proteins. Various bulk and single-particle techniques, each with its advantages and disadvantages, have been used to measure the structure and geometry of viruses.

Bulk techniques measure the ensemble-average properties of viruses and cannot reveal the heterogeneous characteristics of the particle population. They often require prohibiting large amounts of viruses, and lack the resolution and/or the capacity for direct interpretation. X-ray diffraction (XRD) could determine the molecular composition of viruses down to atomic-level resolution^[2] but requires relatively large quantities of ultra-pure virus particles to form well-organized crystals of sufficient size that are stable enough under intense X-ray beams. Nuclear Magnetic Resonance (NMR) requires extensive sample purification and isotopic labeling, and the complete structural determination of most virions remains beyond its reach.^[3] Optical

1. Introduction

The geometrical shape and mechanical properties of microscopic biological entities – including macromolecules, viruses, bacteria,

purification and isotopic labeling, and the complete structural determination of most virions remains beyond its reach.^[3] Optical

K. Li, R. K. Sharma, T. Marjanovic, S. Garaj

Department of Physics
National University of Singapore
Singapore 119077, Singapore
E-mail: slaven@nus.edu.sg

K. Li, A. Shah, P. S. Doyle, S. Garaj
Singapore-MIT Alliance for Research and Technology Centre
Singapore 138602, Singapore
E-mail: pdoyle@mit.edu


K. Li, A. Shah, P. S. Doyle
Department of Chemical Engineering
Massachusetts Institute of Technology
Cambridge, MA 02142, USA

R. Adkins

Department of Physics
University of California
Santa Barbara, CA 93106, USA

S. Garaj
Department of Biomedical Engineering
National University of Singapore
Singapore 117583, Singapore

S. Garaj
Department of Material Science and Engineering
National University of Singapore
Singapore 117575, Singapore

 The ORCID identification number(s) for the author(s) of this article can be found under <https://doi.org/10.1002/admi.202300385>

© 2023 The Authors. Advanced Materials Interfaces published by Wiley-VCH GmbH. This is an open access article under the terms of the Creative Commons Attribution License, which permits use, distribution and reproduction in any medium, provided the original work is properly cited.

DOI: 10.1002/admi.202300385

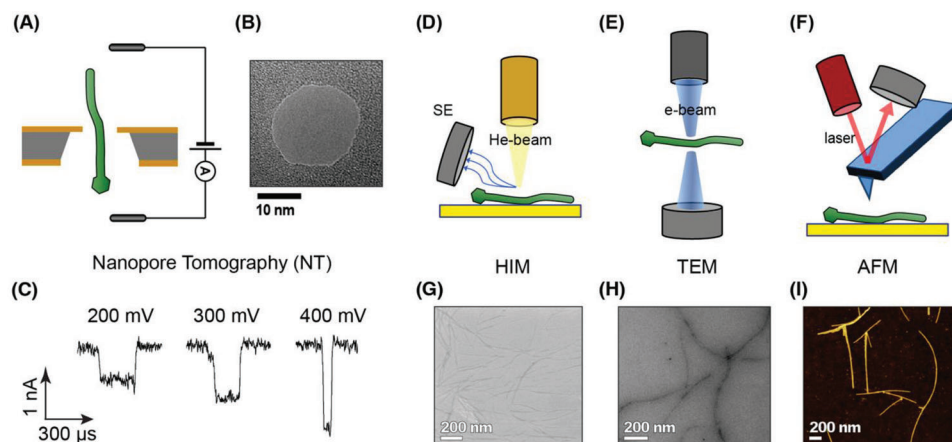


Figure 1. Schematic diagram of the experimental systems: A) NT for morphological measurement of *fd* virus, B) TEM image of a nanopore in silicon nitride (SiN_x) membrane, C) Representative current blockade signals (translocation events) during *fd* translocation through a nanopore, D) HIM, E) TEM, F) AFM, and G) HIM images of *fd* dried on silica surfaces, H) Negative stain TEM images of *fd* virus, and I) AFM tapping-mode height images.

methods based on static/dynamic light scattering (S/DLS) measure effective virion sizes in solution^[4] under the assumption of spherical and homogeneous populations of particles, and hence lack precise size and shape information.

Single-particle methods, such as Transmission Electron Microscopy (TEM) and Atomic Force Microscopy (AFM), produce images of individual viruses but have limited statistics, require long preparation times, and can potentially induce distortions in the virus shapes. The low statistics make it difficult to sample rare configurations in heterogeneous samples – a similar problem inherent to the bulk techniques.

In this work, we have implemented and benchmarked two new methods for measuring the geometrical parameters of viruses with a nanometer-scale resolution – Nanopore Tomography (NT)^[5] and Helium Ion Microscopy (HIM)^[6]. By exploring optimal operating conditions and systematic errors, a particular emphasis has been placed on precision metrology and high throughput measurements rather than simply observing or fingerprinting the viruses. These methods are critically compared to our measurements with TEM and AFM, as well as the other results from the literature.

A nanopore sensor consists of a single nanoscale pore perforating a solid-state membrane that separates two chambers filled with an aqueous salt solution (**Figure 1A**). When a voltage is applied across the membrane, the measured ionic current passing through the nanopore depends strongly on the pore geometry and its immediate surroundings. When a single, charged biomolecule is electrophoretically captured by the pore, it translocates through the nanopore, reducing the cross-sectional area available for the ionic flow. The shape and magnitude of the resulting transient drop in the ionic current (current blockade ΔI_B) is a sensitive measure of the geometric and chemical properties of the translocating object. Nanopores have been used to detect DNA molecules,^[7–9] sequence DNA,^[10] explore the proteins,^[11] viruses,^[12,13] and other biological objects.^[14]

With a successful proliferation of nanopore DNA sequencing technologies in many life-science laboratories,^[10] the term “nanopore detection” is often appropriated for the methods of genomic detection using nanopore sequencing – for example, virus

nanopore detection would be associated with the viral metagenomic studies. This could lead to miscommunication in interdisciplinary settings. To clarify the terminology, we will use the term NT for the measurements of the non-genomic, physio-chemical attributes of biological objects using nanopores. In a narrower sense, it will refer to the detection of geometrical attributes, as discussed in this paper.

NT is a single-particle technique that measures geometrical parameters of viruses *in-operando* (in the aqueous environment), requires minimal sample preparation, and has a large throughput – bridging the gap between single-particle and ensemble-average techniques and probing the heterogeneity of particle samples. It is important to understand its limitations and optimal operating parameters that would a) minimize systematic errors and b) emphasize the geometrical properties of the viruses over their chemical properties. Recently, nanopores have been used to detect and fingerprint viruses and explore their nanoscale dynamics.^[13,15–23] However, these studies were employed in experimental regimes where the chemistry and surface charge of the virus have notable contributions in the nanopore signal generation,^[24] making them unsuitable for metrology (see below). Their goal was to get a distinguishable output signal from various viruses, even though the surface charge defines most of the signal (see later discussion). The questions remain – could NT be used to robustly determine the geometric parameters of a virus without artifacts arising from chemistry? How do NT results compare to the other established single-particle measuring techniques?

HIM is the newest member of the family of scanning beam techniques,^[25–27] akin to Scanning Electron Microscopy (SEM), but using focused helium ions (He^+) as the imaging probe, rather than electrons. While the imaging resolution of SEM is insufficient for efficient virus metrology, we show here that HIM virus imaging has a resolution approaching that of the negative-stain TEM. This is due to reduced interaction volume and reduced charging from the He^+ probe in HIM, as compared to electrons in SEM.^[28] HIM has a much shorter sample preparation time and faster imaging than TEM, resulting in noticeably better statistics and throughput. HIM is gradually being introduced as a method

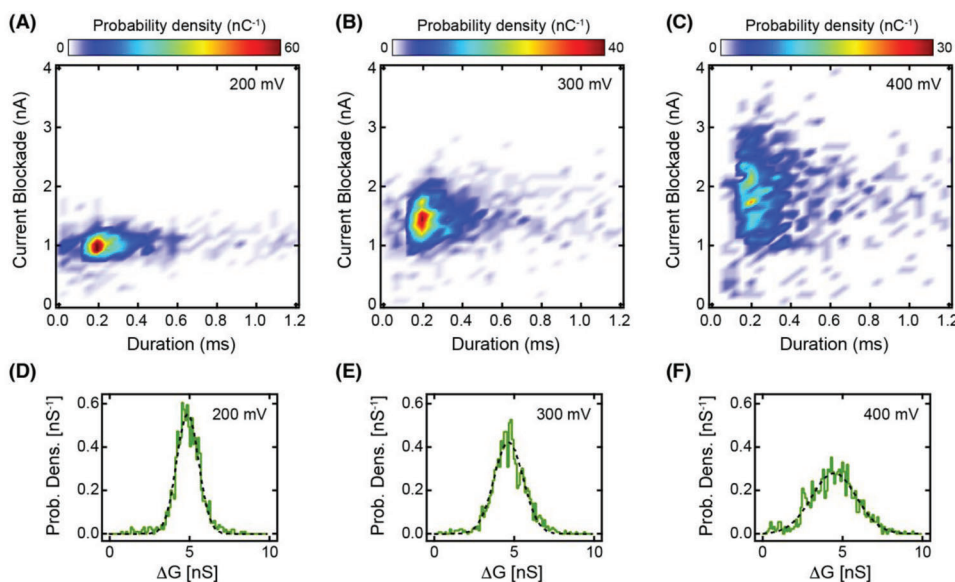


Figure 2. A–C) Scatter plots of translocation time versus current blockade, for *fd* translocation, and D–F) normalized distribution of conductance blockades, for *fd* measured by NT for different voltages. Black dashed curves are Gaussian fits to the experimental data (green curves).

for imaging viruses,^[27,29] and here we have quantified the measuring limits using a virus with intricate features.

The model system for our studies is the *fdY21M* variant of the filamentous *fd* virus.^[30] *fd* is an ideal model system – the virus has been thoroughly analyzed using other imaging techniques; its long filament is easy to find and image, while the small lateral dimension of the virus helps to scrutinize the limits of the metrology.

2. Results

2.1. Nanopore Tomography (NT)

Nanopores were fabricated in a pre-thinned area of free-standing SiN_x membrane on a Si-SiN_x chip, using ablation by the focused electron beam in the TEM. Figure 1B shows the transmission electron micrograph of the resulting nanopore with a diameter of $D = 25.3 \pm 0.8$ nm. The nanopore chip was inserted and sealed between two nanofluidic half-cells (*cis* and *trans* chambers), containing an aqueous solution of potassium chloride KCl at the molar concentration of $C = 1$ M, buffered with 50 mM Tris and 10 mM EDTA (pH = 8.3). As we applied voltage across the membrane, using two Ag/AgCl electrodes inserted in each chamber, we observed the baseline level of ionic current through the nanopore. The nanopore fabrication and ionic measurements followed the previously reported procedure.^[31] From the linear ionic current–voltage (*I*–*V*) curve (see Figure S1, Supporting Information), we calculated the thickness of the membrane as $L = 25.2 \pm 0.3$ nm, which is in the range of estimated thickness targeted by our nanofabrication process.

Viruses were prepared at a concentration of $33 \mu\text{g mL}^{-1}$ (≈ 0.15 nM) by standard biological procedures.^[32] The *fd* viruses were introduced in the *cis* chamber and electrophoretically driven through the nanopore upon application of the voltage across the membrane. As individual viruses translocated through the

nanopore, they excluded a specific volume of the electrolyte, leading to a characteristic current drop that encodes the tomographic information from the virus. Representative examples of such current blockade signals for the translocating *fd* viruses, for an applied voltage of $V_B = \{200, 300, 400 \text{ mV}\}$ are shown in Figure 1C. Since the *fd* virus has a long and uniform filamentous structure, the resulting NT signals have a uniform current drop. Close to 4000 virus translocation events were recorded and parameterized by the total translocation time, T_R and the average magnitude of the current blockade, ΔI_B which is the measure of the virus diameter.

Figure 2A–C shows the density maps of the virus translocation events, parameterized with ΔI_B and T_R . At bias voltage $V_B = 200$ mV (Figure 2A), we observed a tight grouping of the events in the parameter space. The remaining long tail in the distribution of the translocation times T_R is likely due to stick-slip interaction between viruses and nanopore surface, which affected an insignificant fraction of the events. The spread in ΔI_B is likely due to noise level in the baseline current measurements and off-axis translocations at higher voltages. The probability distribution of the conductance blockade $\Delta G_B = \Delta I_B / V_B$, associated with the given density map, is shown in Figure 2D. The distribution was fitted with a Gaussian, yielding an expected value of $\Delta G_B = 4.9 \pm 0.7$ nS, which is used to calculate the virus diameter. The observed spread in blockade levels results in the spread of the calculated virus diameters that are similar, often better, than for the other metrology techniques as discussed later.

As we increased the bias voltage, we observed a progressive increase in the spread of ΔI_B in the density maps of the translocation events (Figure 2B–C). From the associated probability distribution (Figure 2E–F), we see that the expected value of the ΔG_B does not change much with the voltage. Still, the width of the distribution does (see Figure S2, Supporting Information). In the rest of this study, we will use the translocation data for the bias

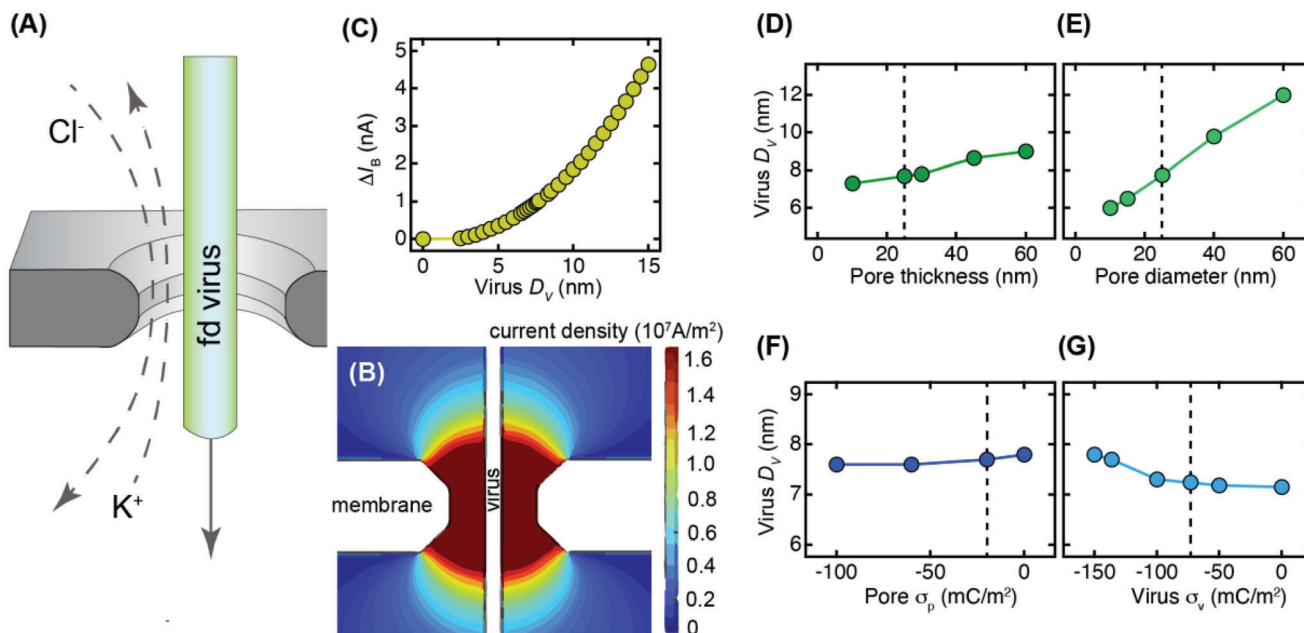


Figure 3. A) Schematic for *fd* translocation through the nanopore, B) contour plot of the current density in the pore vicinity, C) calculated current blockade for different virus diameters, and variation in calculated diameter with D,E) geometrical and F,G) physicochemical parameters at a high salt concentration (1 M KCl). Vertical dashed lines indicate baseline parameter values for each case.

voltage $V_B = 200$ mV, as it shows the lowest spread, and represents the optimal experimental conditions.

To extract the dimensions of the virus from the current blockade signal, we performed finite-element numerical calculations of the virus translocation using Navier–Stokes and Poisson–Nernst–Planck formulations with appropriate boundary conditions^[33–35] in the cylindrical coordinate system (Figure 3A, also see Supporting Information for further details). In the model, we include the known geometry of the pore (thickness $L = 25$ nm, diameter $D = 25$ nm) and its assessed surface charge $\sigma_p = -20$ mCm⁻².^[34]

We model the *fd* virus as a straight, rigid cylinder of diameter D_v carrying a uniform linear charge density of per unit length $\lambda = 10$ e nm⁻¹^[36] centered within the nanopore. Figure 3B shows the distribution of the ionic current density through the nanopore blocked by the virus, calculated for KCl salt concentration of $C = 1$ M. We obtain the current blockade ΔI_B as a function of the virus diameter (Figure 3C) by subtracting the overall ionic current of the blocked pore from the ionic current of the open pore. Comparing the measured and calculated values for the current blockade, we obtain the virus diameter, $D_v = 7.2 \pm 0.5$ nm. The simpler analytical but approximative models for calculating current blockade^[37,38] in the nanopore are not sufficiently precise for our application, as the approximation is too crude and they do not completely account for the effects of the realistic geometry, surface charges, and the contribution of the access resistance.

To make NT an effective metrology instrument and establish its robustness, we have established the optimal virus detection parameters, where any systematic error is reduced, and the variability in the setup parameters minimally impacts the results. The accuracy in determining D_v is affected by the uncertainty in the geometrical and surface charge parameters that are input to

our simulation model (membrane thickness L , pore diameter D , pore surface charge σ_p , and virus surface charge σ_v). How would the variations in those parameters affect the deduced virus diameter? To answer this question, we vary one of the parameters while keeping all others constant. Using the experimental current blockade data, we calculated the evolution of the inferred virus diameter D_v , as we varied the value of the investigated parameter over a wide range (Figure 3D–G).

The results show weak dependence of the calculated virus diameter on the thickness of the membrane, with uncertainty $\Theta(L) = \frac{\partial}{\partial L} D_v \approx 0.04$ nm nm⁻¹ (Figure 3D). Since the thickness of the nanopore is generally well controlled in the nanofabrication process, down to the nanometer scales, the $\Theta(L)$ will not translate to any noticeable error in D_v .

The uncertainty in the nanopore diameter has a more pronounced effect on the accuracy of the calculated virus diameter D_v (Figure 3E) with $\Theta(D) = \frac{\partial}{\partial D} D_v \approx 0.12$ nm nm⁻¹. In our studies, we intentionally employ thin nanopores with a low thickness-to-diameter aspect ratio ($L/D \leq 1$), where enhanced current density at the pore edge leads to a higher sensitivity on geometry.^[39] However, a thin pore allows for better diameter control and reproducibility during fabrication, while the measurements of the nanopore diameter under the TEM are precise with $\delta D_p \approx 0.8$ nm. To ensure the consistency of all the geometrical parameters of the nanopore and their invariance during the experiments, we continuously monitor the open pore ionic current. With all this in mind, we dismiss the pore diameter uncertainty $\Theta(D)$ as a significant source of errors.

The surface charges of the nanopores and viruses are often poorly quantified and vary with pH and salt concentration.^[40] With a proper choice of operating conditions – high salt concentration of $C = 1$ M that results in effective charge

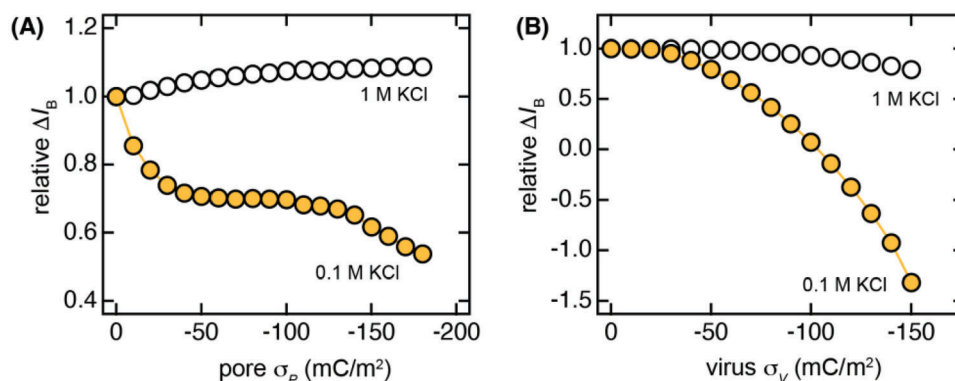


Figure 4. Effect of salt concentration: variation in surface charge densities on the A) pore and B) virus for low (0.1 M KCl) and high (1 M KCl) salt concentrations. The current blockade for each case is normalized with the blockade for zero surface charge case.

screening – our simulations show no discernible dependence of the calculated D_v on the surface charge densities, i.e., $\Theta(\sigma_v) \approx \Theta(\sigma_p) \approx 0$ (Figure 3F,G). Previous experiments with virus translocation through nanopores^[15,17,19,20,22,41] have operated in the regime of low salt concentrations (0.2 M KCl), where the NT signal depends on the physiochemical properties of the viruses. While it is not an appropriate regime for metrology, it has allowed for a detailed investigation of the relevant molecular interactions^[17] and allows for precise fingerprinting and detailed discrimination of the viruses.^[15,16,18–20,22] Karawadeniya et al. aimed to discriminate between AAV viruses with different loads using high molarity 2 mM LiCl solution.^[23] Nonetheless, their signals were over-filtered using low-pass filter with cutoff frequency set at 10 kHz. While this approach might have proven efficacious for fingerprinting applications, it inadvertently introduced considerable distortions to the nanopore signal, rendering it unsuitable for accurate determination of the geometrical parameters.

To demonstrate the effect of the salt concentration on the NT signal, we compare the current blockade deduced from numerical simulations performed at $C = 1$ M and $C = 0.1$ M KCl salt concentrations. We fix the virus diameter at $D_v = 7.2$ nm, bias voltage at $V_B = 200$ mV, and use appropriate nanopore geometry ($D_p = 25$ nm, $L = 25$ nm) and surface charge densities ($\sigma_p = -20$ mC m⁻², $\sigma_v = -70$ mC m⁻²). The surface charge densities on the pore and virus are varied one at a time, while the other parameters are fixed at the specified baseline values. The normalized current blockades for salt concentrations of $C = 0.1$ M and 1 M are presented in Figure 4.

While there is little variability in ΔI_B at $C = 1$ M, there is a significant variation at $C = 0.1$ M, owing to the inefficient screening of charges by counterions. The effect is so drastic that for virus surface charge density, σ_v with magnitudes greater than 100 mC m⁻², the current blockade becomes negative, i.e., the current is enhanced, as reported previously for DNA translocation.^[24] Any small uncertainty in determining the surface charge will result, at low salinity, in an unsustainably large error in calculated virus diameter D_v . The problem is further exacerbated by the fact that the surface charge density of protonizable chemical groups depends on the salt concentration, pH, and dissociation constant, pK_a of those groups,^[34] not to mention the possible effect of ion condensation on the virus surface.^[19,42]

While NT is a rapid, sensitive, and high-throughput technique for viral metrology, there could be some limitations depending on the application. The size information obtained from NT is indirect, but we showed that the determination of the cross-sectional (lateral) dimensions could be quite accurate and robust against the uncertainty of the modeling parameters. Determining the longitudinal parameters (the dimensions along the axis of translocations) could be inaccurate due to the variability in the translocation speed.^[43] Additionally, for non-filamentous viruses, the orientation of the virus during translocation is not controlled. Here we would need to develop a method for tomographic shape reconstruction, based on large sample statistics translocations for different virus orientations.^[11,44]

2.2. Helium Ion Microscopy (HIM)

Helium Ion Microscope creates an image by scanning a focused beam of He⁺ ions, with a lateral resolution of ≈ 0.5 nm, over the surface of the sample.^[6,25,26] The ions interact with the sample material, generating secondary electrons (SE) that leave the sample surface. The position of the scanning beam encodes the spatial information on the image. In contrast, the image intensity is related to the number of secondary electrons counted by a SE detector (see Figure 1D), which is indicative of the local topology and chemistry of the surface under the beam.

HIM operates similarly to SEM, except the scanning probes are He⁺ ions instead of electrons. Since the mass of He⁺ is much greater than that of the electrons, the ions penetrating the material do not deviate too much from the initial trajectory, resulting in a much smaller interaction volume than in the case of incident electrons in SEM. This results in sharp images with a large depth of field on a variety of materials, with significantly better resolution for HIM compared to SEM.

The advantages of HIM extend further. All the scanning beam methods (SEM, HIM, Focused Ion Beam – FIB) suffer from the gradual accumulation of charged ions or electrons on the insulating samples. The charging distorts the incoming scanning beam and could significantly reduce the resolution or render the imaging impossible. In SEM, insulating samples (as biologicals are) should be coated with a thin metallic film, usually gold, to dissipate the accumulating negative charge. The coating obscures

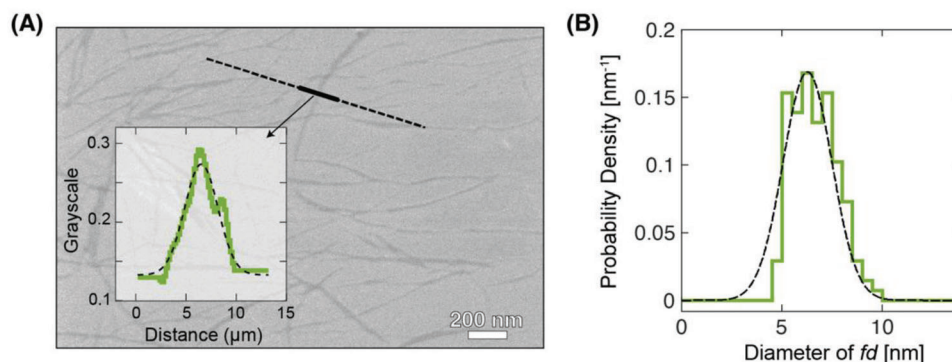


Figure 5. A) HIM image of *fd* dried on a silicon surface. The inset shows a grayscale profile perpendicular to the virus length (black line). B) Normalized distribution of FWHM of *fd* fragment measured by HIM and image processing. HIM imaging was done with the flood gun switched on at an ion beam current of ≈ 2.2 pA (spot-control 4). The sample was tilted by 30° . Distributions for all methods can be found in (Figure S4, Supporting Information).

the fine features of the objects and leads to a loss of resolution. In HIM, no coating is needed; the accumulating positive charge is neutralized by a flood gun, a source of a low-energy electron beam that rasterizes the sample slightly behind the He^+ beam.

Previously, HIM has been used for imaging biological samples,^[25] but not for metrology and determination of the smallest features. Here, we carefully quantify the He^+ beam spread, deconvolute the precise dimensions in the sub-10 nm regime, and discuss the limitations of the technique.

We prepared the samples for HIM by drop casting the aqueous solution of *fd* viruses with a concentration of $33 \mu\text{g mL}^{-1}$ on a pre-cleaned silicon substrate and drying it with a clean nitrogen gun. The sample preparation did not include any surface fixation agents, heavy metal staining, or gold coating, as is often the case in the other single-particle methods (see Experimental Section for details).

Figure 5A shows an HIM image of *fd* viruses (dark filaments) on a silicon surface (light background). For imaging, we used the aperture size 4 (beam current 2.2 pA) to emphasize the high throughput feature of the imaging method. Smaller apertures would lead to a smaller He^+ beam spread and potentially better resolution, but would result in worse image contrast, and longer imaging time. From the image of each virus, we extracted a cross-section intensity profile perpendicular to the length of the viral filament (inset of Figure 5A). The profile could be approximated by a Gaussian with an experimental width $\text{FWHM}_v = 2\sqrt{2\ln 2} \cdot \sigma$ (where, σ is the standard deviation, FWHM_v is full width at half maximum of grayscale profile), which is the convolution of the point spread function (PSF) of the beam and the physical diameter of the virus D_v . The distribution of the measured FWHM_v for many viruses is presented in Figure 5B.

To deconvolute the physical virus diameter D_v from the images, we need to determine the width of the PSF, σ_{PSF} for the given He^+ beam (i.e., the beam spread). To that end, we used two sets of standard gold nanoparticles with diameters narrowly distributed around 15 and 30 nm. We carefully measured their apparent size under the same HIM beam conditions as for imaging viruses. From the apparent size of the calibration nanoparticles, we determined the beam size $\sigma_{\text{PSF}} = 2.5$ nm. Details of the method are discussed in the supplementary information and presented in Figure S3 (Supporting Information). Using the beam

calibration σ_{PSF} and the distribution of the FWHM_v , we determined the diameter of the *fd* virus from HIM measurements, $D_v^{(\text{HIM})} = 7.2 \pm 1.1$ nm. The uncertainty in the diameter arises from the width of the distribution of measured FWHM_v values in Figure 5B. The spread in the distribution could be attributed mainly to limited image quality at the sub-10 nm scales, and it is informative of the accuracy of this metrology method.

As an imaging technique, HIM demonstrates low charging effects, minimal sample damage, high surface contrast, increased depth of field, and a small beam spot size (i.e., a high-imaging resolution). It requires less sample preparation as compared to electron microscopy. Opaque and non-conductive samples could be imaged without metal coatings or stains, and the resolution could approach the one in stained TEM – all at an increased measuring throughput compared to electron microscopy techniques.

When measuring features below 10 nm, such as *fd* virus diameter, a proper beam deconvolution should be applied to deduce small dimensions correctly. The ablation rate of the sample under the He^+ beam is relatively low, even for soft biological materials; it would have minimal effects on the precise measurements of the virus diameters.^[45]

2.3. Transmission Electron Microscopy (TEM)

Over the past few decades, many previously unknown virus families have been examined with negative-stain TEM. Negative-stain TEM provides qualitative morphological information on viral capsids and has been widely used in viral diagnostics.^[46,47] Viral capsids were stained with heavy metal salts before TEM imaging. As shown in Figure 1H, negative staining increases the density of the area surrounding the *fd* particles for enhanced contrast, making the viruses lighter than the background. Images of negatively stained samples are informative but have limited resolution and could be distorted by drying effects and chemical fixations. Sample preparation is a critical part of TEM: not only must samples be carefully obtained, isolated, and purified, but the aqueous samples must be converted to solids and fixed on TEM substrates. Occasionally, negatively stained samples were visibly crushed, collapsed, or distorted^[48] due to drying and chemical fixations, but those artifacts could be more subtle, and harder to pinpoint.

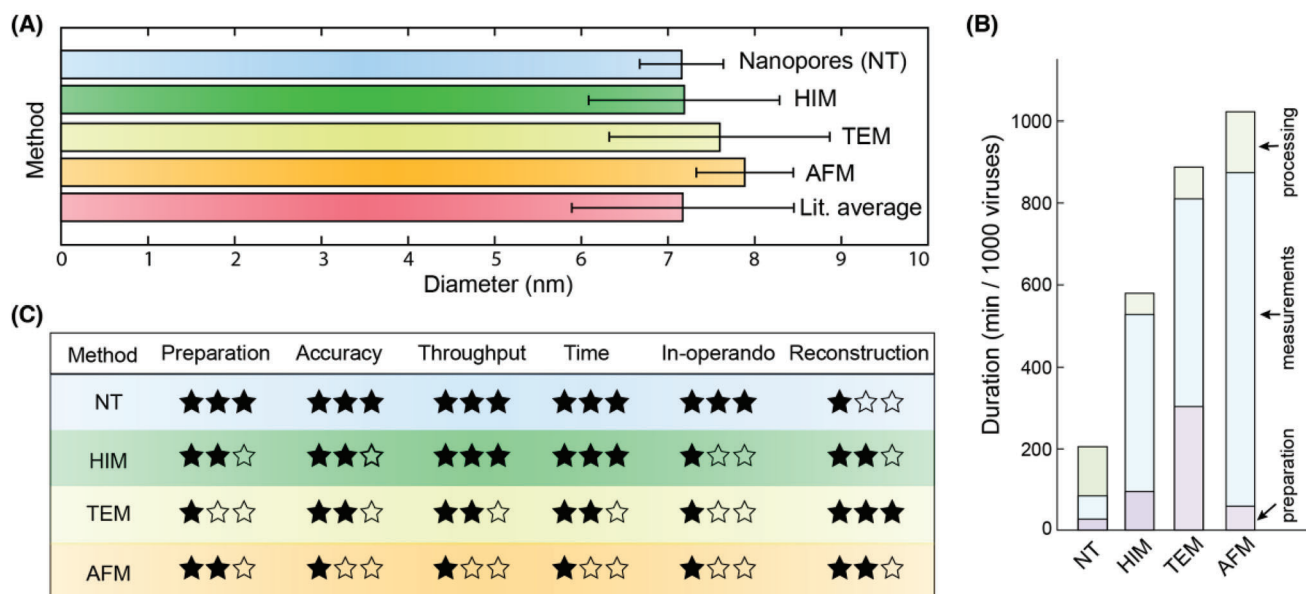


Figure 6. A) Statistical analysis of *fd* diameters measured by four different methods: NT, HIM, TEM, and AFM. These are compared against diameters reported in the literature (Lit. average).^[55–59] Error bars are the standard error of the mean. NT exhibits improved accuracy in measurements as seen by the smallest error bar. B) Quantitative comparison of the total duration for sample preparation, imaging, and data analysis steps in each of the methods. C) Qualitative comparison between the four approaches based on relevant method parameters. The ratings are on a scale of three: poor/average/good. For example, high sample preparation time is rated poor (one star), high accuracy or throughput is rated as good (three stars), and so on.

Negative staining is often used as the first characterization tool for the initial characterization of new viruses or strains. More complex TEM methods, such as electron tomography and cryo-preparative methods, could be used for further detailed analysis of viruses. Cryo-EM is undoubtedly the most precise method for measuring the structure of fully formed viral capsids that are very homogeneous and structurally identical. It is the best way to preserve biological objects in a native (or near-native) state. Three-dimensional (3D) capsid reconstructions have been achieved at near-atomic resolution by averaging multiple two-dimensional (2D) images.^[49] However, Cryo-EM required a lengthy sample preparation, imaging and analysis time, and use of costly instrumentation, limiting the reach of the method. It cannot be used to analyze very heterogeneous samples, so negative-stained TEM is often used to reveal sample heterogeneity,

For our benchmarking, we performed negative-stain imaging of our *fd* viruses. The details of the sample preparation, chemical fixation, and staining are discussed in the Methods section. We followed the standard procedures for TEM imaging of filamentous viruses and obtained virus diameter of $D_v^{(TEM)} = 7.5 \pm 1.2$ nm, similar to published results.^[30]

2.4. Atomic Force Microscopy (AFM)

AFM has demonstrated broad potential for imaging viruses.^[50,51] It does not require any special treatment of the samples. The sample can be imaged in air or liquid (including culture medium or buffer) and in situ on the cell surface.^[52] The most significant concern while imaging with AFM is the convolution of the tip profile with the object profile, and the distortion and “squishing” of the viruses by the tip. Tapping-mode AFM is generally used

to reduce the interaction force between the tip and the sample. In addition to topographical imaging, nanoindentation measurements by AFM can test the strength of individual viral capsids. They can also quantify the mechanical impact of genomic encapsulation and capsid protein mutations on viral capsids.^[53]

The disadvantages of AFM include small scanning size, slow scanning speed, and prominent artifacts that could arise from the tip-sample interactions. Due to the variation in tip-to-tip radius of curvature, measuring in-plane dimensions directly by AFM can be inaccurate. The measured height of the object is not affected by the lateral tip size, but it could be distorted by the force exerted by a tip, especially in the case of soft biological structures. For benchmarking purposes performed tapping-mode AFM imaging of *fd* dried on silica surface using standard preparation and imaging methods (Figure 11 – see Experimental Section). We deduced *fd* diameters from the height analysis in tapping mode images. The obtained value $D_v^{(AFM)} = 7.8 \pm 0.5$ nm is consistent with the values presented in the literature.^[54]

2.5. Comparison of the Virus Metrology Techniques

We have introduced, characterized, and explored the parameter optimization for the two emerging, single-particle techniques for virus metrology – NT and HIM. In Figure 6, we compare their performance with that of the traditional single-particle methods implemented in our laboratory (TEM and AFM), as well as the literature results for the ensemble-average methods (TEB,^[41] XRD,^[42] NS,^[43] and NMR^[44]).

Using NT and HIM, we calculated the diameter of the *fd* virus $D_v^{(NT)} = 7.2 \pm 0.5$ nm and $D_v^{(HIM)} = 7.2 \pm 1.1$ nm, respectively. It is consistent with the values we obtained from TEM and AFM

measurements and the values from the literature (Figure 6A). We see that all the methods have similar accuracy, with some variability in the spread, but there are differences in the other defining features of a methodology, including throughput rate, sample preparation, and operation time, etc.

The accuracy of NT is mainly affected by factors such as uncertainty in pore geometry, surface charge density, salt concentration, etc. Through a series of simulations, we have shown that the operating conditions could be chosen to limit the influence of those uncertainties on the results. The accuracies of HIM and TEM are mainly affected by the beam spread, contrast, and focus, as well as the subsequent image processing. The accuracy of AFM is primarily affected by the size of the AFM tip and the force between the sample and the substrate, etc., which may result in large errors.

For the overall throughput (considering the sample preparation, operation, and post-data processing times), we estimated in Figure 6B the time needed to measure the diameter of a set of 1000 individual viruses, broken down by the different experimental steps. The values are also tabulated and discussed in Supporting Information. The NT measurement has by far the highest throughput, mainly due to its fast measurement time. HIM has a clear advantage over the other direct imaging techniques (TEM, AFM) due to its significantly faster imaging time and simpler preparation method. For all methods, we did not count the time for purification and concentration of virus samples, as it will be very similar for all the techniques, and it will depend on the type and the source of the virus. If we increase the number of measured viruses, mainly the imaging component of the overall metrology time will scale up – increasing the edge of the NT method.

The other features are also important when choosing the appropriate metrology method. In Figure 6C, we evaluate semi-quantitatively, the key features of the four techniques under consideration. TEM and HIM require experienced operators to constantly adjust the focus, astigmatism, and scanning time (current density and dose) to obtain high resolution and contrast. The main disadvantage of AFM is the slow scan speed and narrow scan range, which are throughput bottlenecks.

NT has clear advantages in most of the categories, except for image reconstruction since it is an indirect method. It is good for deducing some critical morphological parameters, such as diameter, but it would require complicated modeling and high statistics if we aim for the full shape reconstruction. One critical advantage of NT over the other techniques is that it could be employed “in-operando”, i.e., viruses are measured freely suspended in the aqueous solution with physiological or varying chemical characteristics (pH, temperature, salinity, chemical agents). The viruses are not affected by chemical preparation, drying, and fixation on the surfaces. Furthermore, we could observe the change in viral morphology based on the varying environmental conditions. For these reasons, NT is enthusiastically being investigated for application in fast, real-time virus fingerprinting.^[60]

3. Conclusion

Small viruses have been studied and accurately imaged at an individual particle level. Using NT, we demonstrate an advance in

the metrology of viruses. The method performs favorably as compared to the other standard imaging techniques. Importantly, we thoroughly establish the sensitivity of the virus diameter on key system parameters using a robust simulation approach. In addition, we present and benchmark HIM as an alternative imaging technique superior to widely used TEM and AFM techniques.

NT is ultrafast, cost-effective, capable of miniaturization, and does not require complicated, time-consuming sample preparation procedures. Despite being a single-particle technique, it can provide a statistically large dataset and enable the study of viral heterogeneity. Meanwhile, we need imaging techniques (HIM, TEM, and AFM) to directly capture the morphological details of the virus, although all these techniques produce varying degrees of distortion, such as sample sputtering with HIM, uneven staining or drying artifacts with TEM, and tip extrusion and sample-to-substrate displacement with AFM.

In conclusion, we demonstrate and benchmark the application of HIM and NT as high-throughput techniques to image and extract useful morphological information for viruses. This study serves as a proof-of-concept for the use of NT to characterize the geometrical features of small viruses and discusses its optimal operating conditions and limitations.

4. Experimental Section

Nanopore Fabrication Process: A 525- μm -thick silicon wafer coated with 300-nm-thick low-stress silicon nitride SiN_x film on both sides was used. The free-standing silicon nitride membranes were fabricated by opening a window in SiN_x film on one side of the wafer, using photolithography and deep reactive ion etching (DRIE) of the wafer. This was followed by the anisotropic wet etching of silicon in 33% KOH solution, resulting in free-standing SiN_x membranes. With an electron beam lithography, a 300-nm-diameter circular area was patterned on the membrane, followed by DRIE etching to reduce the thickness further. The thickness of the pre-thinned area could be reproducibly tuned down to 20 nm. Next, TEM (a JEOL 2010F electron microscope operating at 200 kV) was used to sputter a nanopore at the center of the thinned region using tightly focused electron beam. The nanopore size was tuned by adjusting the electron beam intensity and the beam exposure time. Using this and related techniques, we could reproducibly fabricate the nanopores in the diameter range $D_p = 5 - 300$ nm, to match the sizes of different viruses.

fd Translocation through a Nanopore: The nanopore chips were treated with piranha solution for 1 hour, then mounted between two nanofluidic half-cells filled with the aqueous salt solution. An Ag/AgCl electrode was inserted into each half-cell and connected to a current amplifier (Axon Axopatch 200B with Digidata 1440B data acquisition system). This enabled us to apply a constant voltage difference V across the membrane and record the resulting ionic current. The apparatus was placed inside a grounded Faraday cage for better ambient electromagnetic screening. Further details of the experimental setup have been previously explained.^[31]

The virus samples were diluted to a $33 \mu\text{g mL}^{-1}$ (≈ 0.15 nM) virus concentration in 1 M KCl, 50 mM Tris and 10 mM EDTA (pH = 8.3) aqueous solution, and then injected into the reservoir on the *cis* side. Measurements were performed for transmembrane voltages in the range of 200 – 400 mV. When voltages were applied below 200 mV, the translocation rate of viruses became too small to attain any useful statistics. The rate of translocation for viruses was in the range of 10 per second. The separation between event was much smaller than the translocation time, making unlikely the coincidental translocation of multiple viruses.

The signal was conditioned using four-pole low-pass Bessel filter operating at 100 kHz cutoff frequency, and digitized using a 250 kHz sampling rate. All subsequent analyses of event durations and amplitudes were carried out using MATLAB scripts.

Continuum Simulations of *fd* Translocations: The continuum simulations were performed in COMSOL Multiphysics software package. Nanopore was modeled as a pore with diameter D in an insulating membrane with thickness, L . The surface charge density^[34] inside the nanopore, $\sigma = -20 \text{ mC m}^{-2}$ was used. The virus was modeled as a straight, rigid cylinder of diameter D_v , and carrying a uniform linear charge density $\lambda = 10 \text{ e nm}^{-1}$.^[36] The *fd* translocation experiments were performed at a 1 M KCl salt concentration at three different voltages, and the mean current blockade values for each case are reported in Supporting Information.

Due to the presence of electrical double layers at the charged surfaces, there were steep gradients in concentration, velocity, and potential near the pore surfaces. Therefore, an appropriate mesh size must be chosen for the numerical solver to converge. The length scale for minimum mesh size scales as the Debye length, λ_D in the system. Extremely fine free triangular elements around the electrically charged virus and pore surfaces accurately capture the behavior in the Debye layer region (Figure S5A, Supporting Information). The remaining simulation domain consisted of coarser triangular mesh elements. With the increasing computational costs of exceedingly small mesh, the convergence of ionic current was used to guide the minimum size of mesh (Figure S5B, Supporting Information).

The ion flux or current density, j ($\text{C M}^{-2}\text{s}$ or A M^{-2}) is computed using the following expression:

$$j = F \sum_i z_i N_i = \underbrace{Fv \sum_i z_i C_i}_{\text{Convection}} - \underbrace{F \sum_i D_i \nabla C_i}_{\text{Diffusion}} - \underbrace{\frac{F^2}{RT} \nabla V \sum_i z_i^2 D_i C_i}_{\text{Ion Migration}} \quad (1)$$

where F is Faraday's constant, v is the velocity field, C_i , D_i , z_i are the concentration, diffusion coefficient, and valency of species i , R is the ideal gas constant, T is the temperature, σ is the bulk electrolyte conductivity (S m^{-1}). The corresponding ionic current, I (nA) through a plane perpendicular to the z -axis in a cylindrical, axisymmetric system is calculated as:

$$I_z = \oint j \cdot n_z dS = 2\pi F \int_0^{\frac{D}{2}} \left(\sum_i z_i N_i \right) r dr \quad (2)$$

HIM Imaging of *fd* Viruses: Silicon chips with dimensions of $1 \times 1 \text{ cm}^2$ were soaked in piranha solution (a mixture of three parts concentrated sulfuric acid and one part of 35 wt% hydrogen peroxide solution) at 115°C for 1 hour to decompose organic contaminants and hydroxylate the surface, making the chips highly hydrophilic. Afterward, $50 \mu\text{L}$ of sample solution with a concentration of $33 \mu\text{g mL}^{-1}$ was drop-casted onto the silicon chip and left for 30 min to allow absorption of *fd*. The sample was subsequently rinsed twice with de-ionized water (MilliQ) and blow dried slowly by nitrogen for 10 minutes.

Zeiss Orion Nanofab helium ion microscope was used for imaging. The samples were attached to metal stubs with carbon tape and loaded into the HIM chamber. Acceleration voltage of 30 kV and an aperture of $10 \mu\text{m}$ were used. The spot size was varied between three and four to obtain an ion current in the $2.1\text{--}2.3 \text{ pA}$ range. As the silicon substrate chip had low conductivity, flood gun charge compensation was used, together with line averaging with eight lines and $5 \mu\text{s}$ dwell time.

For precise and efficient extraction of *fd* diameter from images, Scikit-image, Numpy, Scipy, and OpenCV packages in Python were used. Figure 5A demonstrates the original HIM image, which was first converted to grayscale. An active contouring algorithm was subsequently used to find the dark regions in the image and convert it to a binary image. Next, a skeletonization algorithm was applied to thin these dark regions into a single centerline. To separate each centerline section, the junctions were first identified, which were pixels that had more than two surrounding pixels with grayscale value equal to 0 (for a binary image, a pixel with grayscale value equal to 0 means its color is black). Then, each of this centerline section was fitted with a B-spline. Perpendicular to the B-spline, a normal to the section is shown as the black rod in Figure 5A.

The inset in Figure 5A illustrates the grayscale profile along the normal fitted with a Gaussian. The FWHM of each *fd* was calculated from the grayscale profile, assuming it follows the Gaussian shape. The normalized distribution of FWHM values for a set of *fd* viruses is presented in Figure 5B. The exact size of the virus was calculated from the FWHM using calibrated point spread function of the HIM beam, as detailed in Supplementary Material.

TEM Imaging of *fd* Viruses: Virus samples were prepared at a high concentrations ($1.6 \text{ mg mL}^{-1} \approx 80 \text{ nm}$) in 20 mM tris-HCl buffer solution, and then diluted to $33 \mu\text{g mL}^{-1}$ ($\approx 0.15 \text{ nm}$) using 1 M KCl, 20 mM tris, 10 mM EDTA buffer solution. The overlap concentration of *fd* was 0.11 mg mL^{-1} ($\approx 5 \text{ nm}$). Next, the virus samples and 25% Glutaraldehyde solution were mixed at 9:1 ratio to enable fixation of viruses to the TEM grid, resulting in the final virus concentration of $30 \mu\text{g mL}^{-1}$.

To visualize individual virus filaments, negative stain TEM was employed. After increasing the surface hydrophilicity of the TEM grid using glow-discharge setup (Leica ACE200), $20 \mu\text{L}$ of sample solution was drop-casted at $30 \mu\text{g mL}^{-1}$ concentration on the carbon-coated side of the TEM grid. The samples were stained with 1% Gadolinium III Acetate diluted with distilled water. Imaging was performed using a Thermofisher Scientific FEI Tecnai T12 electron microscope operated at 100 kV.

AFM Imaging of *fd* Viruses: The virus samples were diluted to a concentration of $33 \mu\text{g mL}^{-1}$ ($\approx 0.15 \text{ nm}$) in 0.1 M KCl, 20 mM tris, 10 mM EDTA buffer solution. Silica chips with dimensions of $1 \times 1 \text{ cm}^2$ were cleaned with Piranha to be used as substrates. The samples were prepared using the same casting, drying, and rinsing method as for the HIM preparation (described above).

All AFM measurements were recorded in the air using a Bruker FastScan microscope operated in tapping mode at room temperature. Gwyddion software was used for image processing and ImageJ software for accurate numerical measurements of height.

Supporting Information

Supporting Information is available from the Wiley Online Library or from the author.

Acknowledgements

K.L. and A.S. contributed equally to this work. This research is supported by the National Research Foundation, Prime Minister's Office, Singapore under its Campus for Research Excellence and Technological Enterprise (CREATE) program, through the Singapore MIT Alliance for Research and Technology (SMART): Critical Analytics for Manufacturing Personalised-Medicine (CAMP) Inter-Disciplinary Research Group. S.G. acknowledges support from Agency for Science, Technology and Research (A*STAR) Singapore under its Advanced Manufacturing and Engineering (AME) Programmatic grant (Award A18A9b0060). R.A. acknowledges the funding support from NSF-DMR-1905384. S.G. acknowledges support from Ministry of Education Singapore (MOE-T2EP50221-0018). A.S. and P.S.D. acknowledge the MIT SuperCloud and Lincoln Laboratory Supercomputing Center for providing HPC resources that have contributed to the simulation results reported within this paper. The authors thank Zvonimir Dovic for fruitful discussions and support.

Conflict of Interest

The authors declare no conflict of interest.

Data Availability Statement

The data that support the findings of this study are available from the corresponding author upon reasonable request.

Keywords

helium ion microscopy, nanopores, structural characterization, structural imaging, virology, virus metrology

Received: May 16, 2023

Revised: July 27, 2023

Published online:

- [1] D. W. Thompson, *J. Philos.* **1945**, 42, 557.
- [2] N. Verdaguier, D. Garriga, I. Fita, *Subcell. Biochem.* **2013**, 68, 117.
- [3] M. G. Mateu, *Structure and Physics of Viruses: An Integrated Textbook*, Springer, Dordrecht, The Netherlands **2013**.
- [4] P. Kondylis, C. J. Schlicksup, A. Zlotnick, S. C. Jacobson, *Anal. Chem.* **2019**, 91, 622.
- [5] M. Tsutsui, Y. He, K. Yokota, A. Arima, S. Hongo, M. Taniguchi, T. Washio, T. Kawai, *ACS Nano* **2016**, 10, 803.
- [6] B. W. Ward, J. A. Notte, N. P. Economou, *J. Vac. Sci. Technol. B, Microelectron. Nanometer Struct. Process. Meas. Phenom.* **2006**, 24, 2871.
- [7] J. J. Kasianowicz, E. Brandin, D. Branton, D. W. Deamer, *Proc. Natl. Acad. Sci. USA* **1996**, 93, 13770.
- [8] J. Li, D. Stein, C. McMullan, D. Branton, M. J. Aziz, J. A. Golovchenko, *Nature* **2001**, 412, 166.
- [9] S. Garaj, W. Hubbard, A. Reina, J. Kong, D. Branton, J. A. Golovchenko, *Nature* **2010**, 467, 190.
- [10] D. Deamer, M. Akeson, D. Branton, *Nat. Biotechnol.* **2016**, 34, 518.
- [11] E. C. Yusko, B. R. Bruhn, O. M. Eggenberger, J. Houghtaling, R. C. Rollings, N. C. Walsh, S. Nandivada, M. Pindrus, A. R. Hall, D. Sept, J. Li, D. S. Kalonia, M. Mayer, *Nat. Nanotechnol.* **2017**, 12, 360.
- [12] L. Yang, T. Yamamoto, *Front. Microbiol.* **2016**, 7, 1500.
- [13] S. Akhtarian, S. Miri, A. Doostmohammadi, S. K. Brar, P. Rezai, *Bioengineered* **2021**, 12, 9189.
- [14] Y.-L. Ying, Z.-L. Hu, S. Zhang, Y. Qing, A. Fragasso, G. Maglia, A. Meller, H. Bayley, C. Dekker, Y.-T. Long, *Nat. Nanotechnol.* **2022**, 17, 1136.
- [15] J. D. Uram, K. Ke, A. J. Hunt, M. Mayer, *Small* **2006**, 2, 967.
- [16] L. Liu, H. Wu, J. Kong, Q. Liu, *Sci. Technol. Adv. Mater.* **2013**, 5, 2039.
- [17] A. McMullen, H. W. de Haan, J. X. Tang, D. Stein, *Nat. Commun.* **2014**, 5, 4171.
- [18] H. Wu, Y. Chen, Q. Zhou, R. Wang, B. Xia, D. Ma, K. Luo, Q. Liu, *Anal. Chem.* **2016**, 88, 2502.
- [19] A. J. McMullen, J. X. Tang, D. Stein, *ACS Nano* **2017**, 11, 11669.
- [20] A. Arima, I. H. Harlisa, T. Yoshida, M. Tsutsui, M. Tanaka, K. Yokota, W. Tonomura, J. Yasuda, M. Taniguchi, T. Washio, M. Okochi, T. Kawai, *J. Am. Chem. Soc.* **2018**, 140, 16834.
- [21] A. Darvish, J. S. Lee, B. Peng, J. Saharia, R. VenkatKalyana Sundaram, G. Goyal, N. Bandara, C. W. Ahn, J. Kim, P. Dutta, I. Chaiken, M. J. Kim, *Electrophoresis* **2019**, 40, 776.
- [22] M. Taniguchi, S. Minami, C. Ono, R. Hamajima, A. Morimura, S. Hamaguchi, Y. Akeda, Y. Kanai, T. Kobayashi, W. Kamitani, Y. Terada, K. Suzuki, N. Hatori, Y. Yamagishi, N. Washizu, H. Takei, O. Sakamoto, N. Naono, K. Tatematsu, T. Washio, Y. Matsuura, K. Tomono, *Nat. Commun.* **2021**, 12, 3726.
- [23] B. I. Karawdeniya, Y. M. N. D. Y. Bandara, A. I. Khan, W. T. Chen, H.-A. Vu, A. Morshed, J. Suh, P. Dutta, M. J. Kim, *Nanoscale* **2020**, 12, 23721.
- [24] R. M. M. Smeets, U. F. Keyser, D. Krapf, M.-Y. Wu, N. H. Dekker, C. Dekker, *Nano Lett.* **2006**, 6, 89.
- [25] M. S. Joens, C. Huynh, J. M. Kasuboski, D. Ferranti, Y. J. Sigal, F. Zeitvogel, M. Obst, C. J. Burkhardt, K. P. Curran, S. H. Chalasani, L. A. Stern, B. Goetze, J. A. J. Fitzpatrick, *Sci. Rep.* **2013**, 3, 3514.
- [26] T. Wirtz, O. De Castro, J.-N. Audinot, P. Philipp, *Annu. Rev. Anal. Chem.* **2019**, 12, 523.
- [27] M. Schmidt, J. M. Byrne, I. J. Maasilta, *Beilstein J. Nanotechnol.* **2021**, 12, 1.
- [28] G. Hlawacek, V. Veligura, R. van Gastel, B. Poelsema, *J. Vac. Sci. Technol. B, Microelectron. Nanometer Struct. Process. Meas. Phenom.* **2014**, 32, 020801.
- [29] G. M. Almeida, M. Leppänen, I. J. Maasilta, L.-R. Sundberg, *Res. Microbiol.* **2018**, 169, 488.
- [30] E. Barry, D. Beller, Z. Dovic, *Soft Matter* **2009**, 5, 2563.
- [31] R. K. Sharma, I. Agrawal, L. Dai, P. Doyle, S. Garaj, *Nano Lett.* **2021**, 21, 3772.
- [32] J. Sambrook, E. F. Fritsch, T. Maniatis, *Molecular Cloning: A Laboratory Manual*, 2nd ed., Cold Spring Harbor Laboratory Press, Long Island, NY, USA **1989**.
- [33] S. Levine, K. Robinson, W. R. Fawcett, *J. Electroanal. Chem. Interfacial Electrochem.* **1974**, 54, 237.
- [34] D. P. Hoogerheide, S. Garaj, J. A. Golovchenko, *Phys. Rev. Lett.* **2009**, 102, 256804.
- [35] B. Lu, D. P. Hoogerheide, Q. Zhao, D. Yu, *Phys. Rev. E, Stat. Nonlin. Soft Matter Phys.* **2012**, 86, 011921.
- [36] K. Zimmermann, H. Hagedorn, C. C. Heuck, M. Hinrichsen, H. Ludwig, *J. Biol. Chem.* **1986**, 261, 1653.
- [37] S. W. Kowalczyk, A. Y. Grosberg, Y. Rabin, C. Dekker, *Nanotechnology* **2011**, 22, 315101.
- [38] W. Tang, J. P. Fried, R. D. Tilley, J. J. Gooding, *Chem. Soc. Rev.* **2022**, 51, 5757.
- [39] S. Garaj, S. Liu, J. A. Golovchenko, D. Branton, *Proc. Natl. Acad. Sci. USA* **2013**, 110, 12192.
- [40] S. H. Behrens, D. G. Grier, *J. Chem. Phys.* **2001**, 115, 6716.
- [41] A. McMullen, H. W. de Haan, J. X. Tang, D. Stein, *Phys. Rev. Lett.* **2018**, 120, 078101.
- [42] S. W. Kowalczyk, D. B. Wells, A. Aksimentiev, C. Dekker, *Nano Lett.* **2012**, 12, 1038.
- [43] B. Lu, F. Albertorio, D. P. Hoogerheide, J. A. Golovchenko, *Biophys. J.* **2011**, 101, 70.
- [44] C. Ying, J. Houghtaling, M. Mayer, *Nanotechnology* **2022**, 33, 275501.
- [45] V. Castaldo, C. W. Hagen, P. Kruit, *Ultramicroscopy* **2011**, 111, 982.
- [46] Y. Zhang, T. Hung, J. Song, J. He, *Sci. China Life Sci.* **2013**, 56, 421.
- [47] C. S. Goldsmith, S. E. Miller, *Clin. Microbiol. Rev.* **2009**, 22, 552.
- [48] D. M. Belnap, in *Bacteriophages: Biology, Technology, Therapy* (Eds: D. R. Harper, S. T. Abedon, B. H. Burrowes, M. L. McConville), Springer International Publishing, NY, USA **2021**, pp. 561–620.
- [49] J. T. Kaelber, C. F. Hryc, W. Chiu, *Annu. Rev. Virol.* **2017**, 4, 287.
- [50] W. H. Roos, R. Bruinsma, G. J. L. Wuite, *Nat. Phys.* **2010**, 6, 733.
- [51] M. Baclayon, G. J. L. Wuite, W. H. Roos, *Soft Matter* **2010**, 6, 5273.
- [52] Y. G. Kuznetsov, A. McPherson, *Microbiol. Mol. Biol. Rev.* **2011**, 75, 268.
- [53] M. Marchetti, G. Wuite, W. H. Roos, *Curr. Opin. Virol.* **2016**, 18, 82.
- [54] X. Ji, J. Oh, A. K. Dunker, K. W. Hipps, *Ultramicroscopy* **1998**, 72, 165.
- [55] H. Frank, L. A. Day, *Virology* **1970**, 42, 144.
- [56] D. A. Marvin, R. L. Wiseman, E. J. Wachtel, *J. Mol. Biol.* **1974**, 82, 121.
- [57] J. Newman, H. L. Swinney, L. A. Day, *J. Mol. Biol.* **1977**, 116, 593.
- [58] J. Torbet, *FEBS Lett.* **1979**, 108, 61.
- [59] A. C. Zeri, M. F. Mesleh, A. A. Nevzorov, S. J. Opella, *Proc. Natl. Acad. Sci. USA* **2003**, 100, 6458.
- [60] A. Arima, M. Tsutsui, T. Washio, Y. Baba, T. Kawai, *Anal. Chem.* **2020**, 93, 215.